

RESEARCH ARTICLE

10.1002/2015JC010819

Special Section:

Forum for Arctic Modeling
and Observing Synthesis
(FAMOS): Results and Synthesis
of Coordinated
Experiments

Key Points:

- The main source of internal ice stress in the CAA is thermal stress
- The thermal stresses are not isotropic due to land confinement in the CAA
- Stresses induced by tidal/inertial oscillations are insignificant in the CAA

Correspondence to:

Y. Hata,
yukie.hata@mail.mcgill.ca

Citation:

Hata, Y., and L. B. Tremblay (2015),
Anisotropic internal thermal stress in
sea ice from the Canadian Arctic
Archipelago, *J. Geophys. Res. Oceans*,
120, 5457–5472, doi:10.1002/
2015JC010819.

Received 11 MAR 2015

Accepted 16 JUN 2015

Accepted article online 19 JUN 2015

Published online 7 AUG 2015

Anisotropic internal thermal stress in sea ice from the Canadian Arctic Archipelago

Y. Hata¹ and L. B. Tremblay¹
¹Department of Atmospheric and Oceanic Science, McGill University, Montreal, Quebec, Canada

Abstract Results from an ice stress buoy deployed near the center of a multi-year floe in the Viscount Melville Sound of the Canadian Arctic Archipelago between 10 October 2010 and 17 August 2011 are presented. The position record indicates the landlocked season was approximately 5 months, from 18 January to 22 June, when the sea ice was fast to Melville Island and Victoria Island. Thermal stresses (ranging from -84 to 66 kPa) dominate the internal stress record, with only a few dynamic stress events (~ 50 kPa) recorded before the landlocked season. Intriguingly, the thermal stresses are isotropic before the landlocked ice onset and anisotropic during the landlocked season. Two possible causes to explain anisotropy in thermal stresses are considered: preferred c axis alignment of the ice crystal, and land confinement associated with the nearby coastline. The orientation of the principal stresses indicates that land confinement is responsible for the anisotropy. The stress record also clearly shows the presence of residual compressive stresses at the melt onset, suggesting a viscous creep relaxation time constant of several days. Finally, results show an interesting reversal in the sign of the correlation (from negative to positive) between surface air temperature and thermal stress after the onset of surface melt. We attribute this to the onset of water infiltration within sea ice after which colder night temperature leads to refreezing and compressive stresses. To the best of the authors' knowledge, this is the first time that anisotropic thermal stresses have been reported in sea ice.

1. Introduction

Internal sea-ice stresses are induced by winds, ocean currents, floe-floe interactions, and surface air temperature fluctuations [Tucker and Perovich, 1992]. Early on, researchers have been mainly interested in estimating ridge building forces and loads on offshore structures for engineering applications [e.g., Comfort *et al.*, 1992; Richter-Menge and Elder, 1998]. To this end, they have focused on sea-ice motion and the resulting dynamical stresses. More recently, the emphasis has shifted toward bridging the gap between large-scale mechanical properties of sea ice and the magnitude of internal dynamic stresses from in situ measurements for the purpose of validating or proposing new sea-ice rheological models [e.g., Lewis and Richter-Menge, 1998; Hutchings *et al.*, 2010]. A clear understanding of the effect of thermal stresses on the mechanical behavior of sea ice in the context of large-scale sea-ice modeling, however, is still lacking.

In the seminal sea-ice dynamics model of Coon *et al.* [1974], the sea ice is considered to behave as an elastic-plastic isotropic material with no bi-axial tensile strength since sea-ice leads are assumed to open freely in divergence (the Arctic Ice Dynamics Joint Experiment, AIDJEX). Later, Hibler [1977, 1979] introduced the Viscous Plastic (VP) sea-ice model in which small elastic reversible deformations are approximated by viscous creep, while maintaining the no-tensile strength (AIDJEX) assumption. This led to a much simpler numerical solution of the governing equation and the VP model quickly became the standard sea-ice model used in the community. Later improvements mainly focused on the development of more efficient numerical solvers [e.g., Hunke and Dukowicz, 1997; Zhang and Hibler, 1997; Lemieux *et al.*, 2008; Lemieux and Tremblay, 2009], and the constitutive equation representing sea-ice interactions remained mostly the same (exceptions: Girard *et al.* [2011], Sulsky and Schreyer [2004], and Tremblay and Mysak [1997]). Note, however, that different numerical approaches allow for the simulation of landfast ice when tensile strength of sea ice is included [see, König Beatty and Holland, 2010, for instance]. Recently, it has been recognized that the AIDJEX assumptions of no tensile strength and material isotropy are inadequate [Coon *et al.*, 2007] and anisotropic rheologies, either with or without tensile strength, have been developed [e.g., Sulsky and Schreyer, 2004; Wilchinsky and Feltham, 2006]. Note that in all models cited above, thermal effects in the sea-ice rheology are not considered.

Early field campaigns aimed at measuring internal sea-ice stresses took place on multi-year ice in the southern Beaufort Sea in the spring of 1986, 1989, and 1991 [Croasdale *et al.*, 1988; Comfort and Ritch, 1990;

Comfort *et al.*, 1992]. These campaigns focused mainly on dynamic stresses, in particular, on large-scale pack-ice-driving force on structures and the estimation of multi-year ice compressive strength. Croasdale *et al.* [1988] provided an estimate of the sea-ice compressive strength of 52 kN/m from a ridge building event that occurred in the proximity of their stress sensors. Comfort and Ritch [1990] reported ridge building forces ranging from 150 to 700 kN/m, and Comfort *et al.* [1992] reported a mean ridge building force of 30 kN/m with a range of 8–71 kN/m.

In the fall of 1988 (18 September to 25 November), Tucker and Perovich [1992] deployed biaxial wire stress sensors [Cox and Johnson, 1983] on first-year and multi-year ice about 300 km northeast of Svalbard, as part of the Coordinated Eastern ARctic EXperiment (CEAREX). The authors report the presence of open water in the vicinity of the floe from visual observations. Two sources of internal ice stress were identified from the measurements: dynamic stresses (tides, inertial oscillation, and floe-floe collision induced by wind) and thermal stresses. Their results show that dynamic ice stresses in multi-year ice floes decrease with distance from the floe edge—from about 180 kPa at the edge of a 1.5 km diameter floe to about 30 kPa 200 m in the interior of the floe. The stress induced by tidal or inertial oscillation ranged between 20 and 50 kPa. They also show that thermal stresses are well simulated using the simple 1-D thermal stress model of Bogorodsky *et al.* [1972], in which thermal stresses are assumed to be isotropic and viscous creep is not considered, despite clear evidence of viscous creep stress relaxation [Bogorodsky *et al.*, 1972, Figure 6].

The first stress measurements on first-year landfast sea ice in the Canadian Arctic Archipelago (CAA) were done southwest of Cornwallis Island in March of 1992 using biaxial wire stress sensors [Lewis *et al.*, 1994]. In this field campaign, they artificially increased the rate of change of internal sea-ice temperature, and therefore thermal stresses, by mechanically removing the snow cover from the ice. The observed thermal stresses (assumed to be equal to the averaged normal stress) are well simulated by the 1-D thermal stress model of Bogorodsky *et al.* [1972], in which viscous creep was included [Lewis, 1993]. Lewis *et al.* [1994] report tensile stresses in first-year ice as large as 120 kPa when surface air temperature changed from -25 to -31°C , following the removal of the snow cover. This shows the sensitivity of internal thermal stresses with changes in the snow cover depth.

In the winter of 1993–1994 (7 October to 21 March), Richter-Menge and Elder [1998] deployed biaxial wire stress sensors in the Beaufort Sea as part of the Sea Ice Mechanics Initiative (SIMI). The observed major principal stresses (defined as positive in compression) show higher-frequency content, typical of dynamic stresses, at the edge of the floe than in the interior, which is dominated by thermal stresses. Richter-Menge and Elder [1998] proposed two methods to separate the thermal and dynamic stresses. They first assumed that high-frequency stresses (periods of the order of hours) represent ice-motion-induced stresses and lower frequency stresses (periods of the order of days) represent thermal stresses. This separation based on frequency was, however, unsuccessful as the residual ice-motion-induced stress still had a high correlation with ice temperature. They then assumed that the minor principal stress (highly correlated with surface ice temperature) represents the thermal stress and the difference between the principal stresses represents the dynamic stresses. The resulting ice-motion-induced stresses exhibit both high and low-frequency variation and they argue that this method provides a good first-order approximation of thermal and dynamic stresses. Finally, they discuss the seasonality of the observed internal stresses in the Beaufort Sea, with a dominance of thermal stresses in the fall and a dominance of ice-motion-induced stresses in the winter.

Several biaxial wire stress sensors were deployed on a 3 km diameter multi-year ice floe during the Surface HEat Budget of Arctic Ocean (SHEBA) field experiment (October 1997 to April 1998) in the Beaufort Sea [Richter-Menge *et al.*, 2002a]. This study focuses only on dynamic stresses, obtained by removing the thermal stress from the total stress time series following the method proposed by Richter-Menge and Elder [1998]. The spatially averaged dynamic stress during the SHEBA experiment is 25 kPa with a maximum value around 60 kPa (compression). The thermal stresses range between -60 and 50 kPa [see Weiss *et al.*, 2007, Figure 2]. Their results and of Richter-Menge *et al.* [2002b] also show that dynamic stresses observed in the interior of the floe are related to the ice deformation at the regional scale, i.e., internal sea-ice stresses increase during periods of ice convergence, and the internal sea-ice stress decreases during periods of divergence.

Five biaxial wire stress sensors were deployed in first-year and multi-year ice in the Beaufort Sea during the Sea ice Experiment: Dynamic Nature of the Arctic (SEDNA), from 5 April to 25 May 2007 [Hutchings *et al.*, 2010]. The stress results confirm the hypothesis of Richter-Menge and Elder [1998] that the minor principal stress (positive in compression) represents thermal stress and that the difference in principal stresses

provides a good estimate of the maximum shear stress associated with ice motion, although it is suggested that more field work is required to confirm that thermal stresses are isotropic. The maximum reported dynamic stress component is approximately 40 kPa, with an average of 10 kPa. The thermal stresses range from -20 to 70 kPa. Note that, in all studies cited above, the thermal stresses are of the same order of magnitude as the dynamic stresses, and thermal stresses are assumed to be isotropic.

In this paper, we present internal ice stress data from an internal Ice Stress Buoy (ISB) deployed in the Viscount Melville Sound in the CAA (10 October 2010 to 15 July 2011). This is the second ISB deployed in the CAA, after the first measurement by *Lewis et al.* [1994]. The prominent landlocked regime in this region of the Arctic is very different from the previously recorded internal ice stresses in the Beaufort and Lincoln Seas, where the sea ice was in constant motion due to wind forcing [e.g., *Comfort et al.*, 1992; *Tucker and Perovich*, 1992; *Richter-Menge and Elder*, 1998; *Richter-Menge et al.*, 2002a].

The observed stresses presented in this paper are dominated by thermal stresses that are well correlated with surface air temperature. Furthermore, we show that the difference in principal stresses (assumed to be equal to the dynamic stress in previous studies) is also correlated with surface air temperature during the landlocked ice season which calls into question the assumption of isotropy of thermal stress in the CAA. We consider two hypotheses to explain the anisotropy in thermal stress: land confinement and c axis alignment of sea-ice crystals with surface ocean currents [e.g., *Tucker et al.*, 1987; *Weeks and Gow*, 1980; *Kovacs and Morey*, 1978; *Stander and Michel*, 1989]. The data presented provide the first reported evidence (to the authors' knowledge) of anisotropy in landlocked sea-ice thermal stresses.

The manuscript is structured as follows. In section 2, we give a general description of the deployment, the sea-ice stress sensor, and the ice stress buoy. The position and stress records are discussed in section 3. The conclusions are summarized in section 4.

2. Field Measurement Program

2.1. Buoy Deployment

An Ice Stress Buoy (ISB) and a Surface Velocity Profiler (SVP) were deployed on a multi-year sea-ice floe on 10 October 2010 at $74^{\circ}15'N$, $108^{\circ}05'W$ in the Viscount Melville Sound of the CAA (Figures 1 and 2). This region is part of the Parry Channel which connects the Arctic Ocean to the west and Baffin Bay to the east. The deployment was conducted with the logistical support of the Amundsen ice breaker, a research vessel operated by the Canadian Coast Guard, as part of ArcticNet leg 3b (7–22 October 2010). The instrumented multi-year ice floe was approximately 2 km in diameter, and covered with old rounded ridges and several refrozen melt ponds. The sea-ice thickness measured at three different locations, within approximately 10 m, ranged from 1.87 m at the ISB stress sensor location to 3.35 m. The ISB was deployed on a local high-point to avoid having the buoy sit in a melt pond during the following melt season [see installation manual for the CRREL ISB, B. Elder]. The floe was surrounded by water covered with a thin layer of newly formed grease ice. The air temperature on the day of deployment was $-5.1^{\circ}C$.

The ISB was installed by drilling a 4 in. (10.16 cm) hole in the floe down to 3 feet (91.44 cm) depth. A 2 in. (5.08 cm) hole was then drilled from the base of the 4 in. hole, to the ocean, to allow water to fill the cavity. The stress sensor was attached to a PVC pipe, and a wood dowel going through the PVC pipe was used to rest the instrument on the ice surface. The sensor-pipe assembly hung vertically down (like a pendulum) from the wood dowel, allowing it to freeze in a vertical position. The stress sensor was deployed 20.3 cm below the 34.3 cm deep freeboard, i.e., at the depth of 54.6 cm from the ice surface (see Figure 3a). The buoy hub was set in the ice about 4 m away from the stress sensor, using a 3 feet (91.44 cm) long 10 in. (25.40 cm) diameter auger. The buoy compass was aligned with the Magnetic North Pole, and the stress sensor (wire 1: see section 2.2) was also aligned with the Magnetic North Pole using a handheld compass. The stress sensor was connected to the buoy hub by a 6 m long cable (see Figure 3a).

The ISB ran autonomously and transmitted data through the ARGOS satellite system every hour, until the buoy stopped transmitting on 17 August 2011. This allowed for the continuous collection of hourly internal ice stresses (at 54.6 cm depth), air temperatures, ice temperatures (at 54.6 cm depth), location, and compass angle over a period of 10 months. The ISB failed to report its position on several occasion starting on 13 July. The blank in the time series were filled with position reported by the SVP deployed a few meters away.

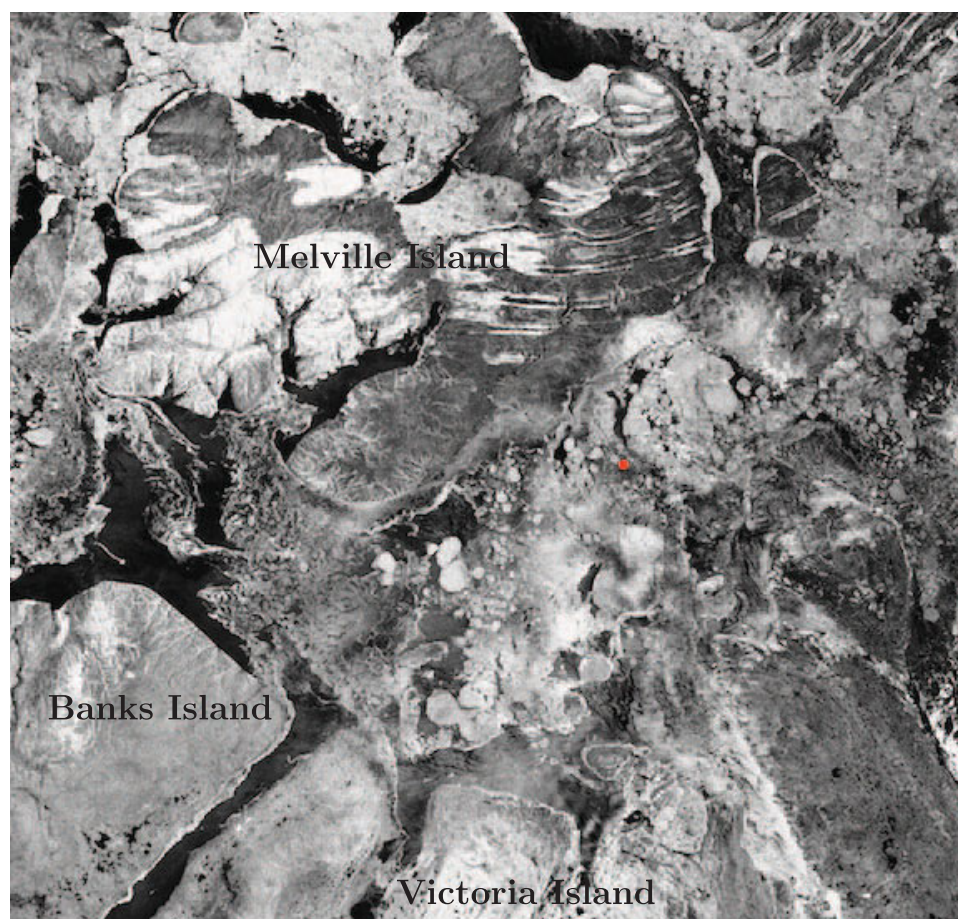


Figure 1. RADARSAT-2 ScanSAR image of the Viscount Melville Sound on 11 October 2010. The location of the deployment is indicated by the red dot. Data and products [copyright] MacDonald Dettwiler and Associates Ltd. (2010)—All Rights Reserved. RADARSAT is an official mark of the Canadian Space Agency.

We note that when the buoy was landlocked, it was located near the north shore of Victoria Island where the coastline to the south is aligned in the northwest-southeast direction (Figure 2a, cf. section 3.1).

2.2. Internal Ice Stress Buoy (ISB) and Surface Velocity Profiler (SVP)

The ISB was manufactured by the Cold Regions Research and Engineering Laboratory (CRREL), and the SVP was manufactured by MetOcean. The ISB is equipped with a stress sensor (model 4350 from GEO-KON), a thermistor used to measure the ice temperature at the depth of the sensor, and a thermistor used to measure 2 m air temperatures (model 107-L05 from Campbell Scientific) (see Figure 3a). The accuracy of both thermistors is 0.01°C . The buoy is also equipped with a Global Positioning System (GPS: model 9601-DGS-LP from NAL Research Corporation) giving the position of the buoy (latitude and longitude) with an accuracy of 10 m and an electric compass (model EZ-Compass-3A V from Advanced Orientation Systems, Inc.) that measures the orientation of the buoy (wire 1) with respect to the Magnetic North Pole with a resolution of 0.08° . The ISB is powered by a lithium battery (TLP-93181/D/OCN2) manufactured by Tadiran Battery. The battery and the data logger (CR1000-ST-SW-NC from Campbell Scientific, Inc.) are included in the buoy hub.

The stress sensor used in this study is a biaxial vibrating wire stress sensor originally designed by Cox and Johnson [1983]. This sensor was successfully used in other Arctic field programs [e.g., Tucker and Perovich, 1992; Richter-Menge and Elder, 1998] and consists of a stiff steel cylinder, 25 cm long, 5.7 cm diameter, and a wall thickness of 1.6 cm. There are three wires and a magnetic coil inside the cylinder. Wires are set 120° from each other across the cylinder diameter (see Figure 3b) and the coil is located under the wires. The wires are plucked by the magnetic coil, inducing a vibration; the periods of each vibrating wire are recorded as raw data.

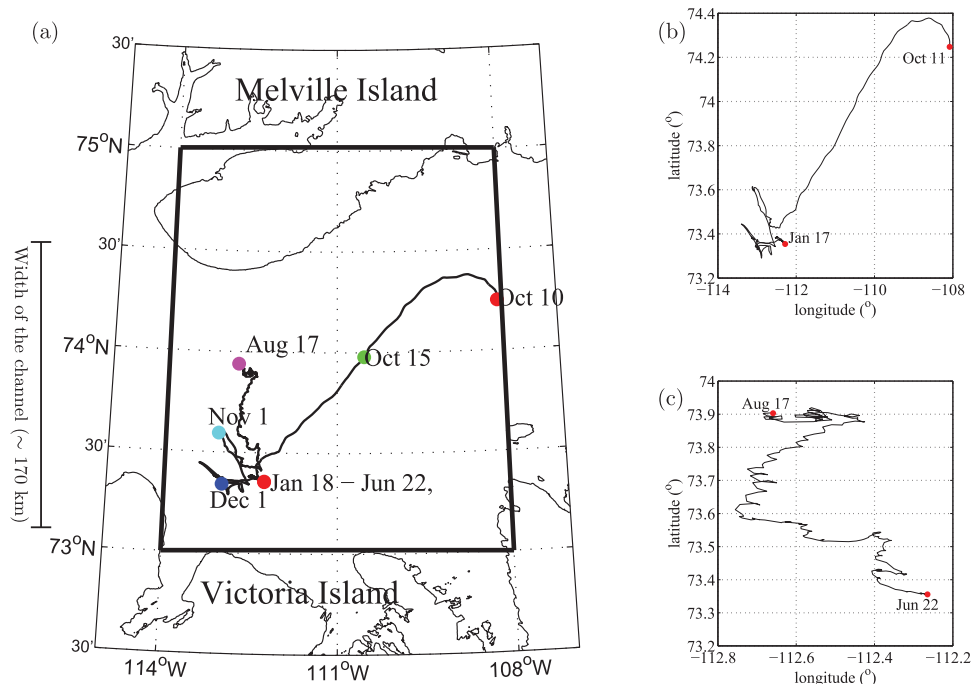


Figure 2. Observed buoy drift from 10 October 2010 to 17 August 2011. Specific dates referred to in the text are also included. The land-locked season is from 18 January to 22 June 2011. Zoom-in of Figure 2b the first drifting season (10 October 2010 to 18 January 2011) and (c) second drifting season (22 June to 17 August 2011). The black solid box delimits the area over which the wind data presented in Figure 7 is averaged (73°N, 114°W–75°N, 108°W).

The elastic deformation of the steel cylinder is related to the period of vibration of each wire and the stresses in the material (in this case, sea ice) are calculated from the cylinder deformation and its Young's modulus [Cox and Johnson, 1983]. This calculation gives the principal stresses (σ_1 and σ_2) and the angle between the minor principal stress (σ_2) and wire 1 (defined positive clockwise). A thermistor located in the proximity of the wires and attached to the cylinder wall is used to correct for thermal effect on the period of vibration. This correction is done during data postprocessing. The error on the principal stresses has

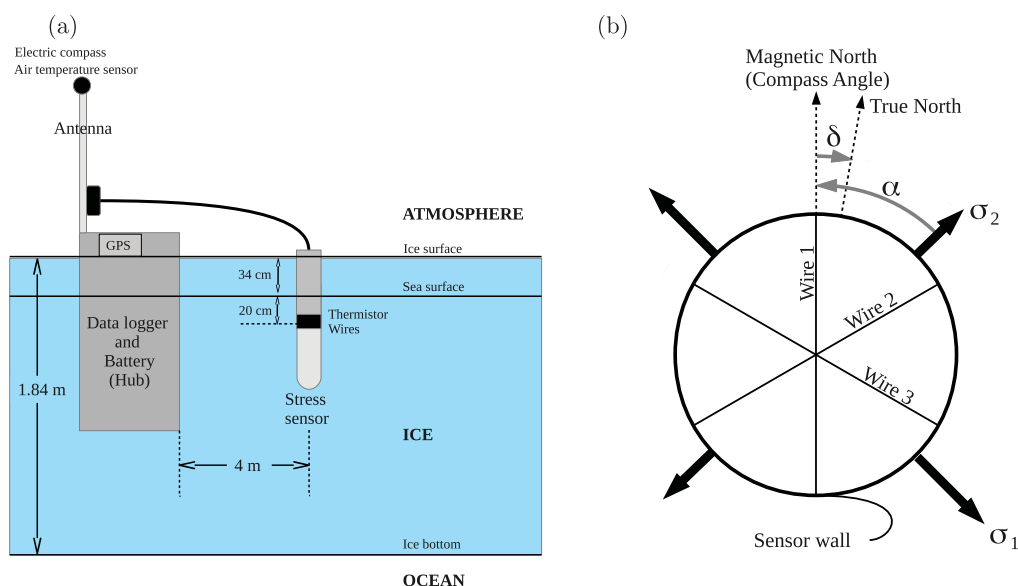


Figure 3. Schematic of Figure 3a the ice stress buoy and (b) the stress sensor. α is the angle between the minor principal stress (σ_2) and wire 1. Wire 1 was aligned with the Magnetic North Pole using a handheld compass during the deployment. The declination angle (δ) between the Magnetic North Pole and the Geographic North Pole in 2010 is approximately 17° in the CAA.

been reduced from 20 kPa to an estimated 5 kPa for a loading range between 0 and 2 MPa, with the use of a superior data-logging system [Cox and Johnson, 1983; Tucker and Perovich, 1992] (see also campbellsci.com). The error in the stress angle is 5°. The conceivable factors for degrading the measurement are the installation and the ice melting around the sensor.

The stress sensor is calibrated in the laboratory prior to deployment. To this end, the relationship between cylinder deformation and period of vibration of each wire, the temperature sensitivity of the wires, and the period of vibration of each wire at 0°C under no load condition are characterized. The laboratory tests are done in an air-filled pneumatic sleeve that applies uniform, hydrostatic pressure. The sleeve is located in a temperature-controlled environmental chamber. The zero-reading of the sensor is sensitive. It can change during shipment and installation, and drifts during the course of a field experiment [Richter-Menge and Elder, 1998]. Ideally, wire periods would be recorded in the field when no mechanical stresses are applied on the sea-ice floe and no significant temperature variations are present. A final calibration would also be made at the end of the experiment by cutting out a block of ice around the sensor when no internal ice stresses are present. This could not be done, however, as the ISB was not recovered.

In this study, we have applied a linear correction to the periods of vibration between 12 October 2010 (Julian Day 285; 2 days after deployment date) and 15 July 2011 (JD 561), 16 days (approximately twice as long as the viscous creep relaxation time constant) after the ice temperature at the depth of the stress sensor reaches the melting temperature of 0°C for the first time. We use the sensor output on that day as the first anchor point corresponding to zero stress despite the fact that some thermal stresses must have been present when the sensor was installed on 10 October when the air temperature was -5.1°C .

The output from the stress sensor is used to calculate the direction of the principal stresses (σ_1 and σ_2) with respect to wire 1 (see Figure 3b). The angle between the principal stresses and Geographical North Pole were calculated from the electrical compass record and a constant magnetic declination angle of 17° between the Magnetic North Pole and the Geographic North Pole in the Viscount Melville Sound in 2010–2011. The compass reading from the ISB was not constant during the landlocked ice season. Instead the reading was correlated with surface air temperature, contrary to the manufacturer specifications (see Figure 4a). While the input voltage of the surface air temperature sensor—whose wire passed just beside the compass on the antenna mast—was programmed to be zero during compass reading, we hypothesize that this may not have been the case. Tension on the wire of the air temperature sensor would produce a magnetic field around the wire and alter the magnetic compass reading. We applied a temperature correction to the compass reading based on a piecewise linear fit between surface air temperature and raw compass reading during the landlocked season when the orientation of the ISB with respect to the Magnetic North Pole was constant. Results from this exercise show that the floe rotated by 10° counterclockwise prior to being landlocked on 18 January (JD 383) (see Figure 4b). Note that there is a sudden shift on JD 530 and a return to pre-JD-530 values on JD 544. The fact that there is no ice motion—as per the GPS data—and that the angle is nearly constant before, during and after the shift suggest a problem in the raw compass angle data as opposed to real rotations of the ice floe.

3. Results and Discussion

3.1. Ice Motion and Landlocked Ice Season

The ISB was deployed approximately 70 km from the south shore of Melville Island and 120 km from the north shore of Victoria Island (see Figure 2a). During the full 10 month life of the buoy, the floe drifted a total distance of 640 km, from 74°15'N, 108°05'W to 73°59'N, 112°38'W between 10 October 2010 and 17 August 2011 (JD 283–594).

After deployment, the ISB drifted 140 km southwest for the first 12 days (JD 283–295) with an average speed of 4.2 km/d, almost parallel to the southern coast of Melville Island. Between 23 October and 18 January (JD 296–383), the floe moved in the northwest and southeast direction. The landlocked season starts on 18 January (JD 383), when the floe stopped drifting. The end of the landlocked season on 22 June 2011 (JD 538) is defined as the moment when the floe starts to rotate as per the compass angle time series (see Figure 4b). Note that the floe starts drifting soon after on 28 June 2011 (JD 544) as per the GPS time series (see Figure 5). From 18 January to 22 June (JD 383–538) the ice was landlocked, and GPS readings from the ISB were constant, except on 10 April (JD 465), when a velocity of 1.4 cm/s (corresponding to a displacement of 52 m in an hour) was observed (see Figure 5). Analysis of the codeployed SVP drift, however, indicates that

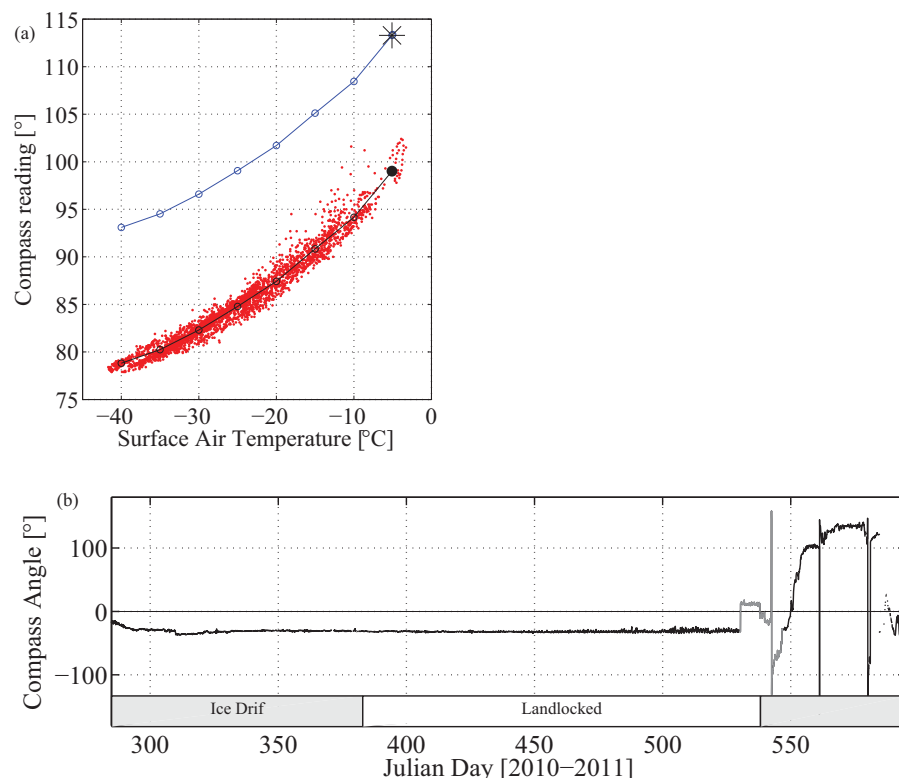


Figure 4. (a) Raw compass reading (red dots) as a function of surface air temperature during the landlocked season (JD 383–556). While the compass was aligned with the Magnetic North Pole at deployment, the initial reading was 113° (marked by the star symbol in Figure 4a) when the surface (1 m) air temperature was -5.1°C . We apply a temperature correction (thin blue line) to the raw compass angles derived from a piecewise linear fit between the raw angles and the surface air temperature (thin black line), with a constant offset of 15° (counterclockwise), equal to $113^\circ - 98^\circ$, the angle from the piecewise linear fit extrapolated to -5.1°C , the air temperature at deployment (solid black dot in a). (b) Buoy orientation relative to the Geographic North Pole after correction. The gray line in the figure shows the data measured when a problem in the compass reading presumably exists (see section 2.2).

this is a false recording. The ISB position indeed was the same after and before this anomalous reading. This is the only obvious false recording of the 10 month time series. All other changes in position recorded by the ISB during the landlocked season are within the measurement error of the GPS, therefore, they are indistinguishable from zero. Between 22 June and 17 August (JD 538–594), the ISB drifted approximately 70 km northward with an average speed of 0.5 km/d. The dates of important events (e.g., Landlocked onset, breakup, etc.) are summarized in Table 1.

3.2. Internal Ice Stresses

The ISB measures the principal stresses (σ_1 and σ_2) and the direction of the principal stresses with respect to the Magnetic North Pole. Note that the mean normal and maximum shear stresses (σ_I and σ_{II} , i.e., the stress invariants) are equal to the average of the two principal stresses and the difference between the two principal stresses divided by two, respectively.

The internal stress data from the ISB, measured at a depth of 54.6 cm from the ice surface, range from -84 kPa (compressive) to 66 kPa (tensile), with 60% of the stresses being positive (tensile; see Figure 6a). The magnitude of the stresses measured at this site are similar to the stresses measured in previous field campaign: CEAREX (~ 150 kPa) [Tucker and Perovich, 1992] and SIMI (~ 60 kPa) [Richter-Menge and Elder, 1998]. After deployment, the stress data shows that the stress sensor was subjected to compressive stresses of around -30 kPa as the seawater in the 4 in. (10.16 cm) borehole froze around the sensor (see the inset in Figure 6a). A few days after the deployment, the compressive stresses were relieved via viscous creep. Following Richter-Menge and Elder [1998] and Hutchings et al. [2010], we first estimate dynamic stresses as the difference between σ_1 and σ_2 assuming thermal stresses are isotropic and their magnitudes are equal to σ_1 (see Figure 7a).

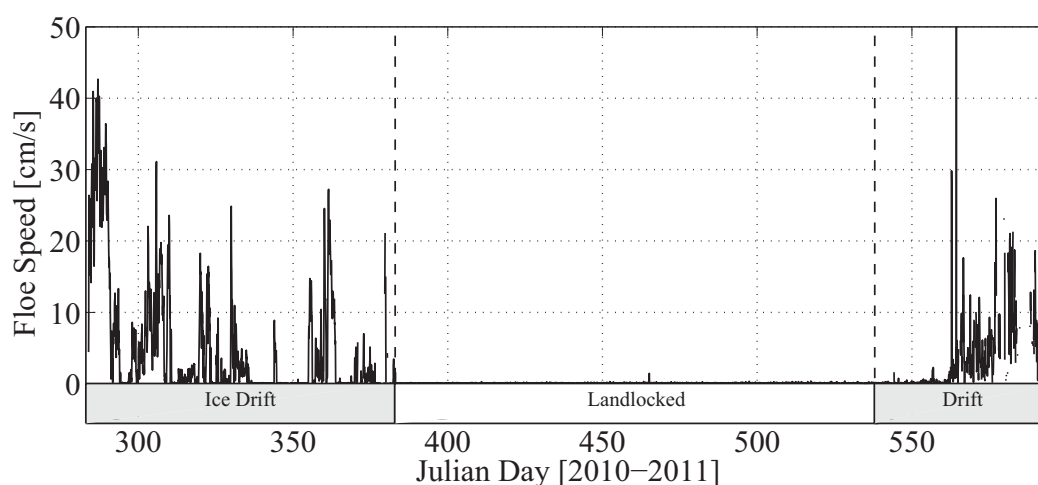


Figure 5. Time series of floe drift speed calculated from observed ISB GPS locations—not including the SVP data used to substitute the false recording and missing ISB data.

3.2.1. Dynamic Stresses

We first note that the difference in principal stresses $\sigma_2 - \sigma_1$, often interpreted as the dynamic stress, does not correlate with wind speed during the landlocked season ($r = -0.01$) or drift season ($r = 0.17$) (see Figure 7). The correlation remains low even if we perform a running-average on the data with a time window of a few days to keep only synoptic-scale variability, or if we only consider data points when the wind direction is close to perpendicular with the nearby coastlines. Instead, $\sigma_2 - \sigma_1$ shows high-frequency fluctuations (indicative of dynamic stresses) between 19 and 23 November (JD 323–327), and between 14 December and 6 January (JD 348–371). We interpret these sudden high-frequency peaks in stresses with floe collisions during the drift season.

The surface air-ice stress is the dominant source of dynamic stress during the landlocked season, when no inertial oscillations or collisions between floes occur. The ocean current velocities in the Viscount Melville Sound are small [Prinsenber and Pettipas, 2008; Wang et al., 2012] and induce relatively low ice stresses. A scale analysis of the total force induced by the wind over a given fetch is equal to $\tau_a L = \rho_a C_a |\mathbf{U}_a|^2 L$ [McPhee, 1975], where τ_a is the surface wind stress, ρ_a (1.3 kg/m^3) is the air density, C_a (3.5×10^{-3} unitless) is the air-ice drag coefficient, and $|\mathbf{U}_a|$ is the surface wind speed. For a characteristic wind speed $|\mathbf{U}_a| = 7 \text{ m/s}$ and fetch $L = 170 \text{ km}$ (the width of the channel), the total surface wind stress is 37 kN. Such wind induced dynamic stresses are much larger than the sensitivity of the stress sensor and should be recorded by the ISB. This suggests that ISBs do not record the slowly varying internal stresses associated with surface wind stresses, and instead only record stresses resulting from mechanical failure and floe-floe interaction.

Table 1. Important Dates

Event	Julian Date	Calendar Date
Deployment	283	10 Oct 2010
Polar night	310–400	6 Nov 2010 to 4 Feb 2011
Landlocked onset	383	18 Jan 2011
Snowmelt onset ^a	524	8 Jun 2011
Ice melt onset ^a	526	10 Jun 2011
Reversal of the correlation between ice temperature and thermal stresses	530	14 Jun 2011
Landlocked breakup	538	22 Jun 2011
Ice reaches isothermal condition (0°C)	545	29 Jun 2011
Noisier internal stress measurement	559	13 Jul 2011
Ice melt reaches sensor depth	561	15 Jul 2011
Buoy death	594	17 Aug 2011

^aThe date for snowmelt onset and ice melt onset are from a simulation of the 1-D multilayer sigma-coordinate thermodynamic model of Huwald et al. [2005] forced with the observed 1 m surface air temperatures.

During the drift season (JD 284–383 and JD 538–561), the power spectrum of $\sigma_2 - \sigma_1$, calculated using a continuous wavelet transform, shows a weak peak at a frequency of 2 day^{-1} associated with tidal and/or inertial oscillations (see Figure 8a). Indeed, the position record of the ISB shows drift tracks in the shape of hairpins during both drift season (JD 283–383 and JD 538–594; see Figures 2b and 2c). A continuous wavelet transform analysis of the floe-drift vectors shows an appreciable peak at frequencies between 1.8 and 2.1 day^{-1} , confirming the presence of tidal/inertial

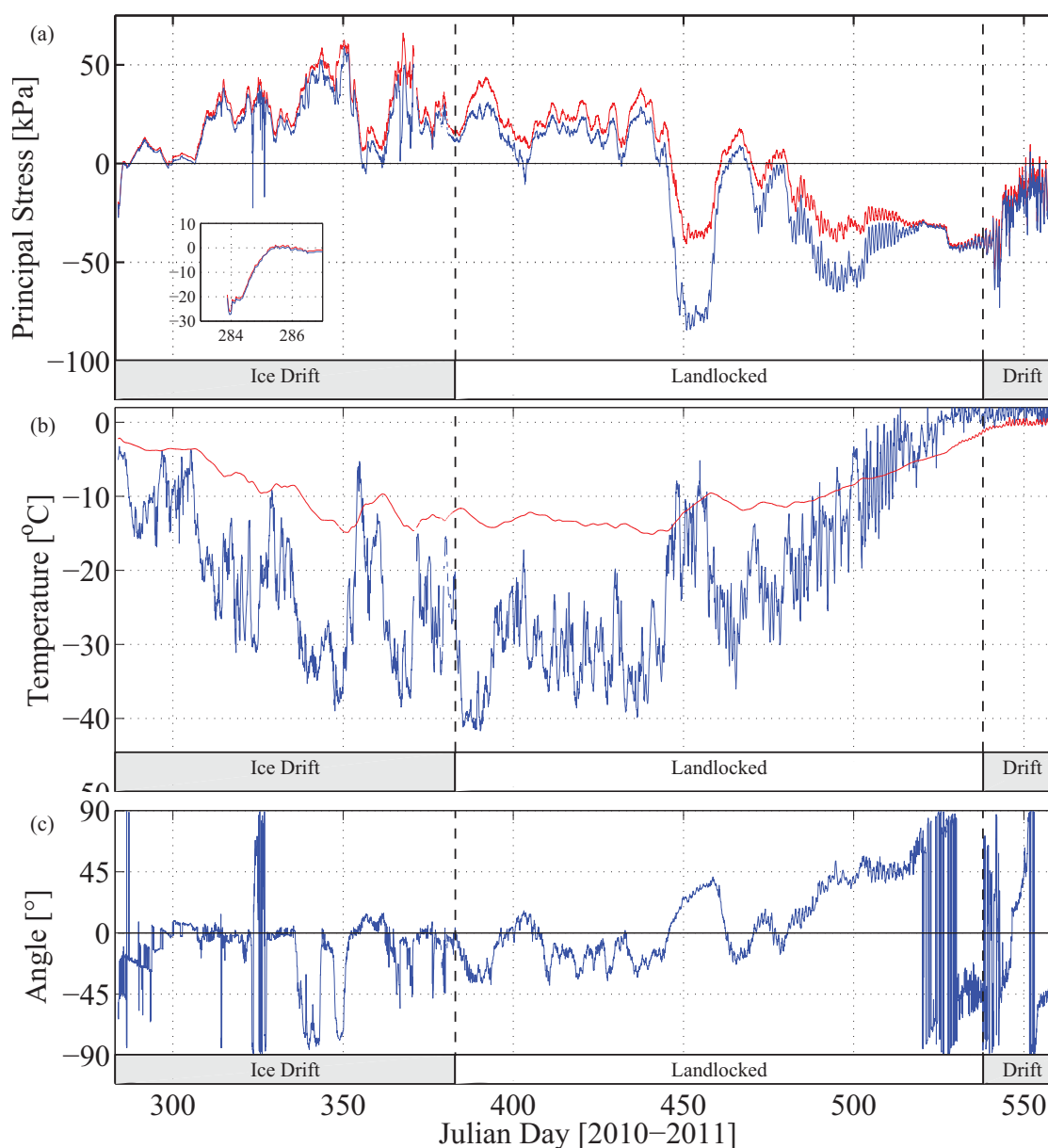


Figure 6. (a) Time series of the major (σ_1 : red line) and the minor (σ_2 : blue line) principal stresses, (b) surface air (1 m: blue line) and wire (red line) temperatures, and (c) corrected angle between the minor principal stress (σ_2) and Geographic North Pole, defined positive clockwise and ranging between $\pm 90^\circ$. Note that the stress angle, shown in Figure 6c, is only meaningful when the stress states are anisotropic ($\sigma_1 \neq \sigma_2$). The insert in Figure 6a shows a zoom-in on the stress for the first few days when the sensor set in the ice.

oscillations (see Figures 8c and 8d). At a latitude of 73°N , the inertial oscillation and tidal signal frequencies are 1.92 and 1.94 day^{-1} , respectively. Following *Gimbert et al.* [2012], we calculated the signed Fourier transform of the buoys velocities. The results confirm that both inertial oscillation (only negative frequency due to clockwise rotation) and tidal oscillation (both positive and negative frequencies) are present (see Figure 9).

During the landlocked season (JD 383–538), there are by definition no inertial oscillations (1.92 day^{-1}) and there is no peak at the tidal frequency (1.94 day^{-1}). The absence of a tidal signal in the second stress invariant ($\sigma_2 - \sigma_1$) during the landlocked season is presumably due to its smaller magnitude. This is in contrast with previous observations by *Tucker and Perovich* [1992, Figure 14], who reported 25–50 kPa stresses associated with tidal and inertial oscillations. When the pack ice is mobile, tides and inertial oscillations result in divergent and convergent sea-ice drift, and hence sea-ice collisions occur [*Holloway and Proshutinsky*, 2007].

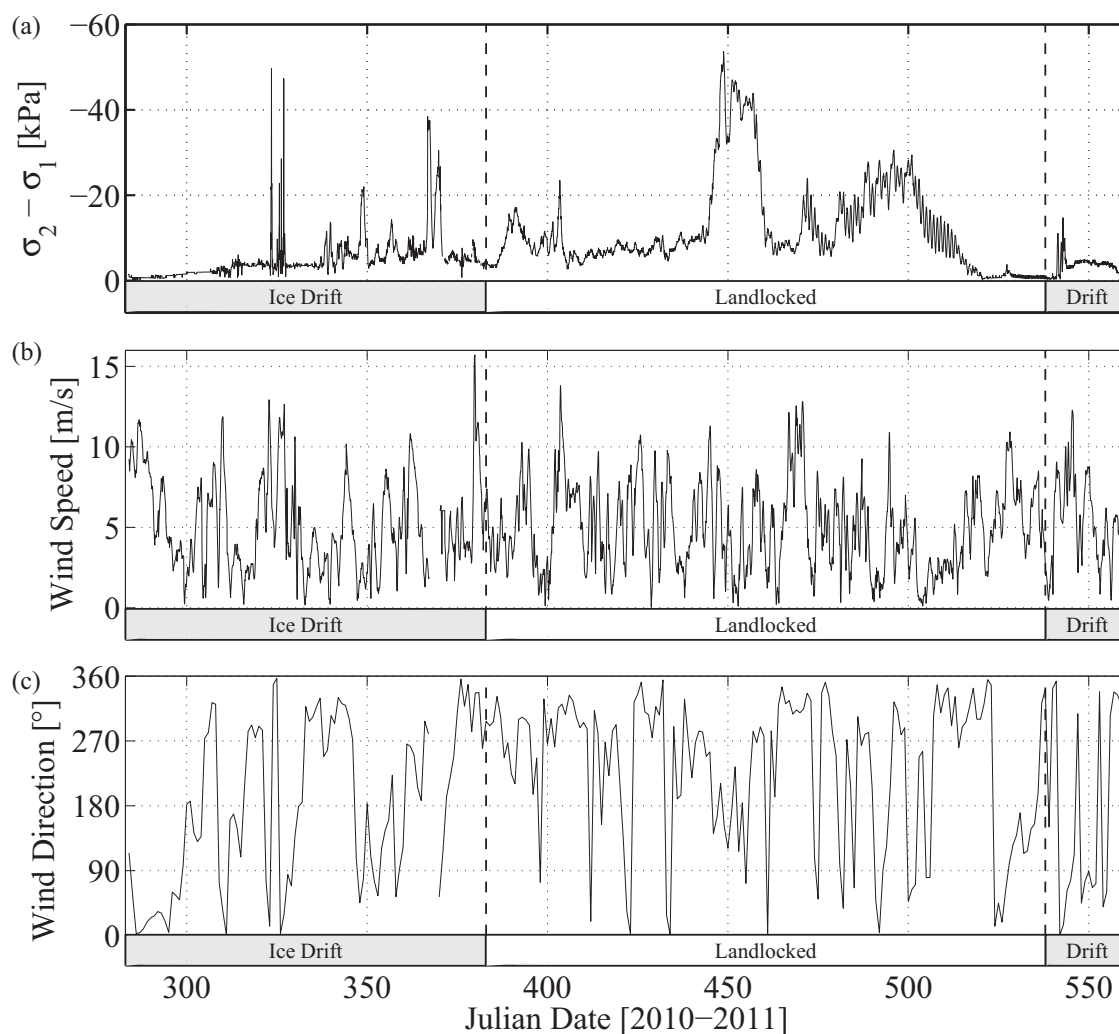


Figure 7. Time series of (a) the difference between the major and minor principal stresses, (b) mean wind speed, and (c) mean wind angle over the region defined in Figure 2. The wind data are from the Canadian Meteorological Center's (CMC) Global Deterministic Prediction System (GDPS) [Smith *et al.*, 2013]. The wind speed and $\sigma_2 - \sigma_1$, often used as a good first estimate of dynamic stress [e.g., Hutchings *et al.*, 2010], are not correlated ($r = -0.01$ during the landlocked season, $r = 0.17$ during the drift seasons).

For the landlocked sea ice in the CAA, tides do not cause floe collisions. Consequently, the stresses induced by tides are not recorded by the sensor.

3.2.2. Thermal Stresses

When air temperature changes, the temperature signal is transmitted through the ice and damped with depth from the surface to the ice base, which remains at the freezing point temperature of -1.8°C . This vertical temperature gradient results in a different amount of thermal contraction or expansion with depth. In the absence of gravitational pull or buoyancy, a floe would bend and curl concave upward due to the vertical differences in horizontal strain, but because of the large aspect ratio (floe length over floe depth), the floe remains flat [Lewis, 1993]. As a result, tensile and compressive stresses develop in the upper and lower parts of a floe, respectively, when surface air temperature decreases.

Thermal stress is the dominant source of internal stresses in the ISB stress record. When the surface temperature decreases (increases) associated with the diurnal, synoptic, or seasonal cycle, tensile (compressive) stress develops in the upper part of the sea ice. The magnitudes of the thermal stress fluctuations associated with the diurnal, synoptic, and seasonal cycle in temperature are approximately 10, 60, and 40 kPa (see Figure 6a). The correlations coefficients (r) between surface air temperature and the observed principal

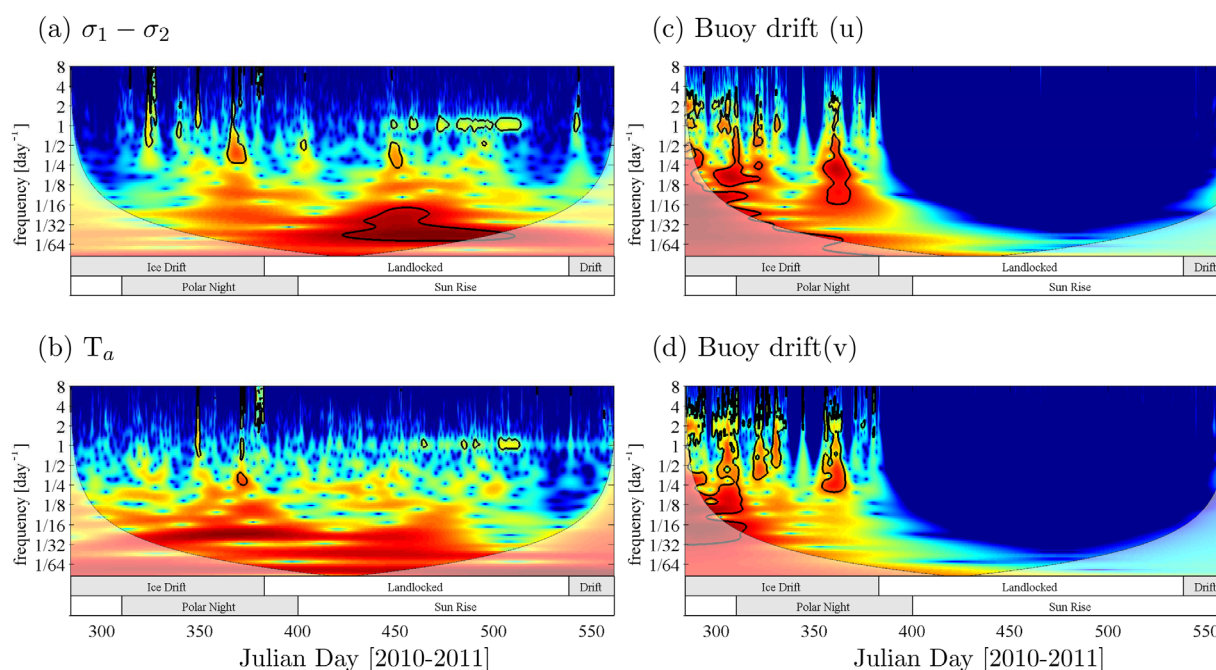


Figure 8. Wavelet power spectrum analysis of (a) $\sigma_2 - \sigma_1$, (b) air temperature, and the (c) u- and (d) v-component of the multi-year ice floe drift. Note that a log scale is used on the y axis. The thick black contour indicates the 5% significance level against red noise and a lighter shade shows the cone of influence subject to edge effects.

stresses (σ_1 and σ_2) for the full 8 month period are -0.76 and -0.63 , respectively (see Table 1 and Figure 10). These results are similar to previous measurements made at a mean depth of 22 cm in drifting multi-year ice by Richter-Menge [1997] and Richter-Menge and Elder [1998]. The maximum lagged correlation (r) between air temperature and σ_1 (σ_2) is -0.78 (-0.66) for a 26 (26) hour lag, the time scale required for the temperature signal to reach the stress sensor at 55 cm depth.

The continuous wavelet spectrum analyses of the principal stresses (results not shown) and air temperature time series (Figure 8b) show two peaks, one at frequencies between 0.3 and 0.5 day^{-1} (synoptic scale) and the other at a frequency of 1 day^{-1} (diurnal cycle). The peak associated with synoptic variability is present during the entire record. The diurnal frequency peak in σ_1 , σ_2 , and surface air temperature is present after 4 February 2011 (JD 400), when the Sun rises above the horizon in the Viscount Melville Sound.

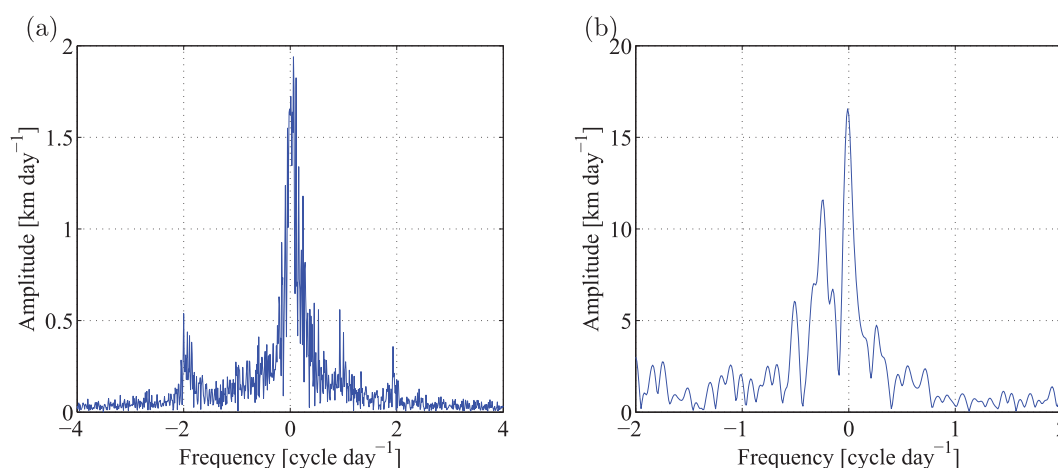


Figure 9. Signed Fourier spectrum analysis on the floe drift for (a) JD 283–383 and (b) JD 538–594. Note that the analysis on the second drift period (JD 538–594) is done using 3 hourly position record of the SVP because the ISB failed to record its position frequently during this period. This limits the frequency range resolved from the data to $\pm 2 \text{ day}^{-1}$.

Table 2. Correlation Coefficients (r) Between Air Temperature and Ice Temperature at the Sensor Depth (-55 cm), and the Principal Stresses (σ_1 , σ_2 , and $\sigma_2 - \sigma_1$) From 10 October 2010 (JD 283) to 15 July 2011 (JD 561)^a

	σ_1	σ_2	$\sigma_2 - \sigma_1$
T_{air}	-0.76 (-0.78 : 26 h)	-0.63 (-0.66 : 26 h)	-0.65^b
T_{ice}	-0.57	-0.39	

^aThe values inside of parentheses are the maximum lagged correlation coefficients (r).

^bThe correlation coefficients (r) between air temperature and $\sigma_2 - \sigma_1$ is calculated for the landlocked season only (JD 383–538) and using the band-pass filtered surface air temperature and $\sigma_2 - \sigma_1$.

ner similar to the compressive stresses recorded when the stress sensor was set in ice on 10 October 2010).

While the multi-year ice floe is drifting (JD 283–382), the thermal stresses are isotropic (σ_1 and σ_2 are approximately equal, see Figure 6a), in accord with the assumption made by Lewis *et al.* [1994], Richter-Menge and Elder [1998], and Hutchings *et al.* [2010]. In this case, the magnitude of the local normal stresses is the same in any reference coordinate system. Therefore, there are no significant shear stresses. During the landlocked season (JD 383–538), differences between the two principal stresses appear. During that period, we observe low-frequency fluctuations in the band-pass filtered $\sigma_2 - \sigma_1$ that correlates with the band-pass filtered surface air temperature ($r = -0.65$, see Table 1). This implies anisotropy in thermal stresses. In this case, the magnitudes of the local normal stresses on two perpendicular planes in the reference coordinate systems are different and shear stresses are present (except on the principal stress axes, by definition).

Two possible factors can explain the difference in principal stresses after the onset of the landlocked season. The first is a preferred c axis alignment of the sea-ice crystals in the direction of the surface ocean currents resulting in different Young's modulus and therefore different thermal stresses in the direction perpendicular and parallel to the coastline. The second is land confinement in the north-south direction, the direction perpendicular to the long axis of the channel.

The c axis is the axis of the common crystal structure of sea ice, the direction in which the ice growth rate and the Young's modulus is also largest. C axis alignment has been observed in the Greenland Sea [Tucker *et al.*, 1987], Kara Sea [Cherepanov, 1971], Alaskan coastline [Weeks and Gow, 1980; Kovacs and Morey, 1978], Pond Inlet [Stander and Michel, 1989], and Allen Bay near Resolute [Parsons *et al.*, 1986]. Weeks and Gow [1978] propose that c axis alignment could be used to derive the mean direction of surface ocean currents in perennially

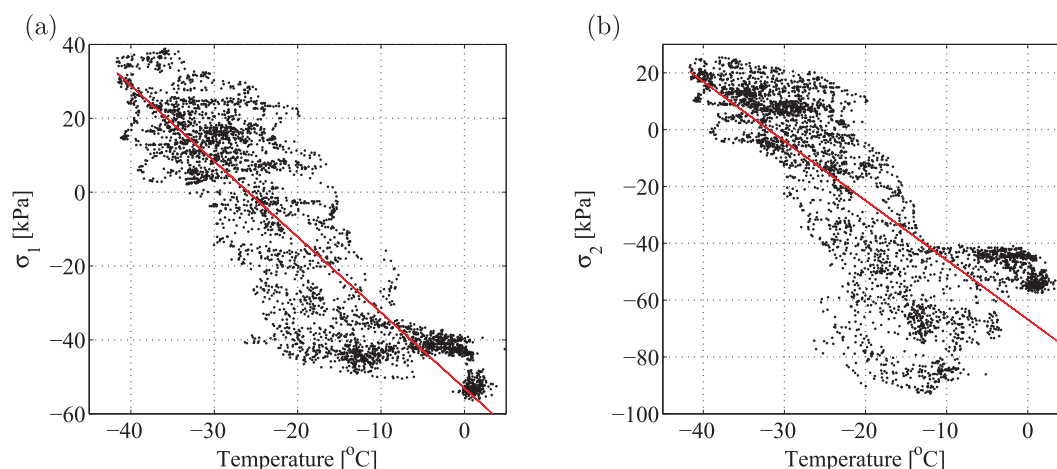


Figure 10. (a) Major (σ_1) and (b) minor (σ_2) principal stresses as a function of surface air temperature.

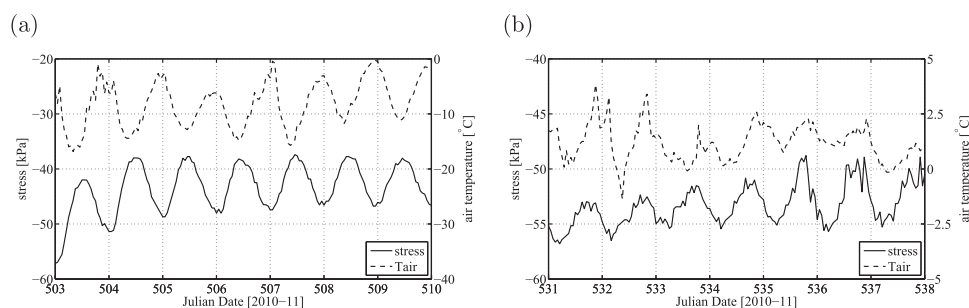


Figure 11. Zoom-in of the surface air temperature and observed first stress invariant ($\sigma_I = \frac{\sigma_1 + \sigma_2}{2}$) (a) before and (b) after the start of the melt season. Note that the sign of the correlation between the two fields reverses between the two time period. We hypothesize that this reversal is due to the start of water infiltration within the sea ice.

ice covered such as the CAA. When the c axis of ice crystals aligns, the directional dependency of the Young's modulus becomes important, leading to differences in principal stresses.

A typical difference in principal stresses due to the preferred c axis alignment is equal to $\Delta E \propto \Delta T$, where ΔE (0.3E [Schulson, 1999]) is the difference in Young's modulus in the direction parallel and perpendicular to the c axis, α (5×10^{-5}) is the coefficient of thermal expansion and ΔT (5°C, JD 450; Figure 6b) is a characteristic ice temperature change at the sensor depth. For a range of observed Young's modulus between 0.3 and 10 GPa, this leads to a difference in principal stress ranging from 22.5 to 750 kPa.

A typical difference in principal stress due to land confinement is equal to $E \frac{\Delta L}{L} = E \alpha \Delta T$, where ΔL is the thermal contraction of an ice slab of length L (170 km, the width of the channel) associated with a characteristic temperature drop ΔT (approximately -5°C). For a range of Young's modulus between 0.3 and 10 GPa, this corresponds to differences in principal stress ranging from 75 to 2500 kPa.

The stresses caused by both c axis and land confinement are therefore large enough to explain the observed difference in principal stress during the landlocked ice season, peaking at 50 kPa on JD450. However, the orientation of the minimum principal stress (σ_2) with respect to the Geographic North Pole will be different in the two cases. In the case of the preferred c axis alignment, the larger stress (in magnitude) will be in the direction parallel to the coastline (-45° from the Geographic North Pole), since this is the direction with the larger Young's modulus. This implies an angle of 45° between the minimum principal stress (σ_2) and the Geographic North Pole at the location of the ISB during the landlocked season when the stresses are tensile (see Figure 12a). When the stresses are compressive, the angle between the minimum principal stress (σ_2) and the Geographic North Pole will be -45° .

In the case of land confinement during the landlocked season, basal friction between the ice and the ocean floor at the coastline will result in larger (smaller) stresses in the direction perpendicular to the coastline when the surface air temperature decreases (increases). This implies an angle of -45° between the minimum principal stress (σ_2) and the Geographic North Pole when the stresses are tensile and an angle of 45° between the minimum principal stress (σ_2) and the Geographic North Pole when the stresses are compressive (see Figure 12b). The stress angle data from the ISB shows an angle of approximately -45° between σ_2 and the

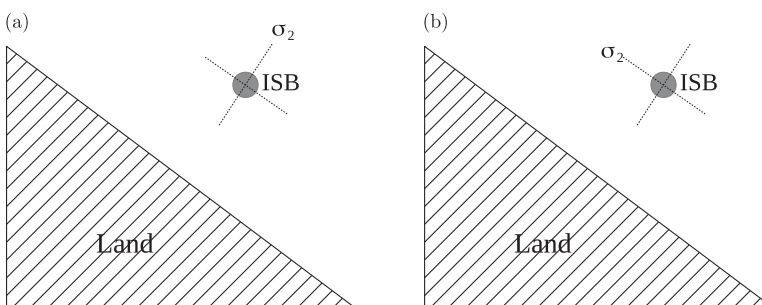


Figure 12. Direction of the minor principal stress (σ_2) with respect to the coastline for the case where c axis alignment (a) and land confinement (b) is responsible for the anisotropy. This is for the case where the surface air temperature is decreasing.

Geographical North Pole when the temperature decreases and the ice is under tensile stress (Figures 6a–6c; JD 385–390, JD 408–445). When the ice is warming and under compressive stress, the angle turns to approximately 45° (Figures 6a–6c; JD 395–405, JD 450–460). Note that the angle data is not well defined in the drift seasons when the stresses are isotropic ($\sigma_1 = \sigma_2$) and there is no directional dependence. We conclude that land confinement, rather than c axis alignment, is responsible for the difference in principal stresses.

We estimate the ice anchoring force by multiplying the difference in principal stress and by a typical ice thickness of first-year ice. Assuming a first-year sea-ice thickness of approximately 2 m, the anchoring force ranges between 35 and –110 kN. Note that the principal stress axis reverse when the stresses change from compressive to tensile, since σ_1 and σ_2 are the minimum and maximum stresses.

Finally, why can ISBs record slowly varying (synoptic time scale) stresses induced by surface air temperature changes when they cannot record stresses induced by surface winds in the absence of fractures and floe collisions remains an open question.

4. Conclusions and Future Work

An internal Ice Stress Buoy (ISB) was deployed on multi-year ice floe in the Viscount Melville Sound on 10 October 2010. A nearly 9 months (10 October 2010 to 15 July 2011) internal sea-ice stress time series and 10 months (10 October 2010 to 17 August 2011) position record were collected. The GPS record from the ISB indicates that the landlocked ice season in the Viscount Melville Sound was approximately 5 months, from 18 January to 21 June 2011.

The observed stress data are highly correlated with changes in surface air temperature and not significantly correlated with the magnitude or the direction of the wind speed. This is in part explained by the smaller wind fetch, the attenuation of dynamic stress from the floe edge to its interior [e.g., *Tucker and Perovich, 1992; Richter-Menge and Elder, 1998*], but more importantly because ISBs record dynamic stresses induced by fracture and the resulting floe-floe collisions. The internal stress time series shows a few dynamic stress events characterized by high-frequency changes in the recorded internal ice stresses associated with floe-floe collisions before the landlocked season between 10 October 2010 and 17 January 2011 (JD 283–382).

The magnitude of the internal thermal stress ranges between –84 and 66 kPa. The magnitude of the dynamic stresses range between –49 and 0 kPa. When the surface air temperature drops, tensile stress develops at the sensor depth (and compressive stress develops in the lower part of the ice slab). This is due to the thermal contraction in the upper part of the ice while the ice in contact with the surface ocean remains isothermal at the freezing point temperature.

Before the sea ice became landlocked, the internal thermal stresses were nearly isotropic. During the landlocked season, significant differences between σ_1 and σ_2 were recorded, yet σ_1 and σ_2 remained highly correlated with surface air temperature. This shows that thermal stresses in landlocked ice in the CAA are not isotropic.

We consider two possible causes to explain anisotropy in thermal stresses: preferred c axis alignment in the ice crystal with surface ocean currents in coastal water leading to different material properties along and normal to the c axis, and land confinement in the northeast-southwest direction induced by the nearby coastlines. The orientation of the principal stress time series with respect to the Geographic North Pole indicates that the effect of land confinement dominates over the effect of the c axis alignment.

The internal ice stress time series also clearly shows the presence of residual compressive stresses at the beginning of the melt season when the sea ice internal temperature is nearly isothermal. The observed internal stress time series suggests a viscous creep relaxation time scale of several days. Recall that four or five time constants are required for the residual stresses to return to zero in a simple first order differential equation of the form $\frac{\partial \sigma}{\partial t} = -\frac{1}{\tau} \sigma$, where τ is the relaxation time constant. This is longer than previously reported values in the literature. This result is also supported by modeling evidence from a 1.5D thermal stress model (results presented in a companion paper in the same issue).

Results also show an interesting reversal in the sign of the correlation (from negative to positive) between diurnal fluctuations in surface temperatures and the recorded internal stresses at 55 cm beneath the ice surface during the melt season. We attribute this change in the sign of the correlation to the onset of water

infiltration within the sea ice (at least to the depth of the sensor). This water freezes at night, expands, and leads to compressive stresses at the sensor depth in a manner similar to the compressive stress that develops when the stress sensor first sets in after installation.

The relative magnitude of thermal stresses compared to the dynamic stresses in the CAA suggests that they may be important to consider in sea-ice rheological models developed for this region. Moreover, the anisotropy in internal stress induced by land confinement (or ice anchoring on nearby shores) leads to differences in internal stresses as large as 50 kPa when large changes in temperature occur. This again will have an impact on the mode of failure of landlocked ice, the shape of the landlocked ice edge, and the timing and location of landlocked ice onset and breakup in the CAA.

Future work addressing some of the questions that are raised in the present analysis should focus on deployment of ISBs on first-year landlocked ice to eliminate the added complexity of stress transmission between first-year and multi-year ice. In particular, measurements of internal stresses at different depth within first-year ice (above and below the zero thermal stress boundary within sea ice, as was done in multi-year ice by Tucker and Perovich [1992] and Richter-Menge and Elder [1998]) should be conducted to further test the hypothesis that ice anchoring on the shore line is responsible for anisotropy. We would expect the vertically integrated thermal stress in landlocked ice to be in tension (compression) when the surface air temperature cools (warms), as opposed to zero as in the case of coastal landfast ice that has a free boundary in the offshore direction. In addition, we propose to repeat the measurements in a different region of the CAA to confirm the results presented in this paper and to core sea ice to verify if *c* axis alignment is indeed present in sea ice within the Archipelago. Finally, we suggest deploying several ice stress buoys on first-year ice in the same region to investigate the spatial variability of thermal and dynamic stress recorded by the stress sensor. We would expect to see a high correlation in thermal stress recorded by different buoys if there are no spatial variability in air temperature, wind, and snow cover depth. In multi-year ice, previous studies have shown that there is a wide variation in the magnitude between dynamic stresses measured even on the same floe a few kilometers apart. Whether this is also the case for thermal stresses measured in first-year ice remains an open question.

Acknowledgments

Y. Hata is grateful to ArcTrain Canada and Québec-Océan for financial support during the course of this work. The buoys deployments were made possible by a generous grant from Ferring Pharmaceutical. We are grateful to ArcticNet and the crew from the Amundsen ice breaker research vessel operated by Canadian Coast Guard and the Polar Continental shelf Program and its staff for their logistic support during the buoys deployments. B. Tremblay is grateful for financial support from ArcticNet, the Natural Sciences and Engineering Research Council (NSERC) Discovery program, Environment Canada Grants and Contribution program, the office of Naval Research (N000141110977), and the Canadian Sea Ice and Snow Evolution (CanSISE) Network funded by NSERC Climate Change and Atmospheric Research program. We thank Jacqueline A. Richter-Menge for useful discussions regarding the postprocessing of the buoy data and for her careful review of the manuscript and helpful comments, and Bruce C. Elder for his technical assistance and useful discussions. We are grateful to Gregory Smith from the Environment Canada for providing the Canadian Meteorological Center's (CMC) global deterministic prediction system (GDPS) high-resolution wind data set, and grateful to Stephen Howell for providing the RADARSAT-2 image. We also thank Erland Schulson for useful discussion regarding the anisotropy of coastal sea ice, Robert Newton and Melany Belzile for their technical assistance with the data processing, and Line Bourdages and James Williams for their careful edit of the manuscript. We thank Jennifer Hutchings for her careful review of the manuscript and helpful comments. The data are publicly available on the CRREL data repository (imb.erdc.dren.mil) or by contacting Bruno Tremblay at bruno.tremblay@mcgill.ca.

References

- Bogorodsky, V. V., V. P. Gavrilov, A. V. Gusev, Z. M. Gudkovich, and A. P. Polyakov (1972), Stressed ice cover state due to thermal wave and related underwater noise in the ocean, in *Proceedings of Ice Symposium*, pp. 28–33, AIRH Translation, Leningrad.
- Cherepanov, N. V. (1971), Spatial arrangement of sea ice crystal structure, *Probl. Arktiki Antarkitiki*, 38, 137–140.
- Comfort, G., and R. Ritch (1990), Field measurement of pack ice stresses, in *Proceedings of 9th International Conference of Offshore Mechanics and Arctic Engineering*, pp. 177–181, Amer. Soc. Mech. Eng., Houston, Tex.
- Comfort, G., R. Ritch, and R. M. W. Frederking (1992), Pack ice stress measurements, in *Proceedings of 11th International Conference of Offshore Mechanics and Arctic Engineering*, pp. 245–253, Amer. Soc. Mech. Eng., N. Y.
- Coon, M., G. A. Maykut, R. S. Pritchard, D. A. Rothrock, and A. S. Thorndike (1974), Modelling the pack ice as an elastic plastic material, *AIDJEX Bull.*, 24, 1–105.
- Coon, M., R. Kwok, G. Levy, M. Pruis, H. Schreyer, and D. Sulsky (2007), Arctic ice dynamics joint experiment (AIDJEX) assumptions revisited and found inadequate, *J. Geophys. Res.*, 112, C11S90, doi:10.1029/2005JC003393.
- Cox, G. F. N., and J. B. Johnson (1983), Stress measurement in ice, *Tech. Rep. 83-23*, Cold Reg. Res. and Eng. Lab., Hanover, Germany.
- Croasdale, K. R., G. Comfort, R. M. W. Frederking, B. W. Graham, and E. L. Lewis (1988), A pilot experiment to measure arctic pack-ice driving forces, in *Proceedings of 9th International Conference on Port and Ocean Engineering Under Arctic Conditions*, pp. 381–395, University of Alaska, Geophysical Institute, Fairbanks.
- Gimbert, F., D. Marsan, J. Weiss, N. C. Jourdain, and B. Barnier (2012), Sea ice inertial oscillations in the Arctic Basin, *Cryosphere*, 6(5), 1187–1201.
- Girard, L., S. Bouillon, J. Weiss, D. Amutrano, T. Fichefet, and V. Legat (2011), A new modeling framework for sea-ice mechanics based on elasto-brittle rheology, *Ann. Glaciol.*, 52(57), 123–132.
- Hibler, W. D., III (1977), A viscous sea ice law as a stochastic average of plasticity, *J. Geophys. Res.*, 82(27), 3932–3938.
- Hibler, W. D., III (1979), A dynamic sea ice model, *J. Phys. Oceanogr.*, 9, 815–846.
- Holloway, G., and A. Proshutinsky (2007), Role of tides in Arctic ocean/ice climate, *J. Geophys. Res.*, 112, C04S06, doi:10.1029/2006JC003643.
- Hunke, E. C., and J. K. Dukowicz (1997), An elastic-viscous-plastic model for sea ice dynamics, *J. Phys. Oceanogr.*, 27, 1849–1867.
- Hutchings, J. K., C. Geiger, A. Roberts, J. Richter-Menge, and B. Elder (2010), On the spatial and temporal characterization of motion induced sea ice internal stress, in *International Conference and Exhibition on Performance of Ships and Structures in Ice*, pp. 1–8, International Arctic Research Center, Anchorage, Alaska.
- Huwald, H., L. B. Tremblay, and H. Blatter (2005), A multilayer sigma-coordinate thermodynamic sea ice model: Validation against surface heat budget of the arctic ocean (SHEBA)/sea ice model intercomparison project Part 2 (SIMIP2) data, *J. Geophys. Res.*, 110, C05010, doi:10.1029/2004JC002328.
- König Beatty, C., and D. M. Holland (2010), Modeling landfast sea ice by adding tensile strength, *J. Phys. Oceanogr.*, 40, 185–198, doi:10.1175/2009JPO4105.1.
- Kovacs, A., and R. M. Morey (1978), Radar anisotropy of sea ice due to preferred azimuthal orientation of the horizontal *c* axes of ice crystals, *J. Geophys. Res.*, 83(C12), 6037–6046, doi:10.1029/JC083iC12p06037.

- Lemieux, J.-F., and B. Tremblay (2009), Numerical convergence of viscous-plastic sea ice models, *J. Geophys. Res.*, *114*, C05009, doi:10.1029/2008JC005017.
- Lemieux, J.-F., B. Tremblay, S. Thomas, J. Sedláček, and L. A. Mysak (2008), Using the preconditioned generalized minimum residual (GMRES) method to solve the sea-ice momentum equation, *J. Geophys. Res.*, *113*, C10004, doi:10.1029/2007JC004680.
- Lewis, J. K. (1993), A model for thermally-induced stresses in multi-year sea ice, *Cold Reg. Sci. Technol.*, *21*, 337–348.
- Lewis, J. K., and J. A. Richter-Menge (1998), Motion-induced stresses in pack ice, *J. Geophys. Res.*, *103*(C10), 21,831–21,843, doi:10.1029/98JC01262.
- Lewis, J. K., W. B. Tucker III, and P. J. Stein (1994), Observations and modeling of thermally induced stresses in first-year sea ice, *J. Geophys. Res.*, *99*(C8), 16,361–16,371, doi:10.1029/94JC01242.
- McPhee, M. G. (1975), Ice-ocean momentum transfer for the AIDJEX ice model, *AIDJEX Bull.*, *29*, 93–111.
- Parsons, B. L., J. B. Snellen, and B. Hill (1986), Physical Modeling and the Fracture Toughness of Sea Ice, *Proceedings of the fifth international mechanics and Arctic engineering symposium*, vol. IV, pp. 358–364, Amer. Soc. Mech. Eng., Tokyo, Japan.
- Prinsenber, S., and R. Pettipas (2008), Ice and ocean mooring data statistics from Barrow Strait, central section of NW passage in Canadian Arctic Archipelago, *Int. J. Offshore Polar Eng.*, *18*, 277–281.
- Richter-Menge, J. A. (1997), Towards improving the physical basis for ice-dynamics models, *Ann. Glaciol.*, *25*, 177–182.
- Richter-Menge, J. A., and B. C. Elder (1998), Characteristics of pack ice stress in the Alaskan Beaufort Sea, *J. Geophys. Res.*, *103*(C10), 21,817–21,829, doi:10.1029/98JC01261.
- Richter-Menge, J. A., S. L. McNutt, J. E. Overland, and R. Kwok (2002a), Relating arctic pack ice stress and deformation under winter conditions, *J. Geophys. Res.*, *107*(C10), 8040, doi:10.1029/2000JC000477.
- Richter-Menge, J. A., B. Elder, J. Overland, and S. Salo (2002b), In situ sea ice stresses in the western Arctic during the winter of 2001–2002, in *Proceedings of the 16th IAHR International Symposium on Ice*, vol. 2, pp. 423–430, Intern. Assoc. Hydraul. Eng. Res., Dunedin, New Zealand.
- Schulson, E. M. (1999), The structure and mechanical behavior of ice, *J. Miner. Met. Mater. Soc.*, *51*, 21–27.
- Smith, G. C., F. Roy, P. Mann, F. Dupont, B. Brasnett, J.-F. Lemieux, S. Laroche, and S. Bélair (2013), A new atmospheric dataset for forcing ice-ocean models: Evaluation of reforecasts using the Canadian global deterministic prediction system, *Q. J. R. Meteorol. Soc.*, *140*, 881–894, doi:10.1002/qj.2194.
- Stander, E. D., and B. Michel (1989), The development of aligned columnar sea ice: A field investigation, *J. Glaciol.*, *35*(120), 217–223.
- Sulsky, D., and L. Schreyer (2004), MPM simulation of dynamic material failure with a decohesion constitutive model, *Eur. J. Mech. A Solids*, *23*, 423–445, doi:10.1016/j.euromechsol.2004.02.007.
- Tremblay, L. B., and L. A. Mysak (1997), Modeling sea ice as a granular material, including the dilatancy effect, *J. Phys. Oceanogr.*, *27*, 2342–2360.
- Tucker, W. B., A. J. Gow, and W. F. Weeks (1987), Physical properties of summer sea ice in the Fram strait, *J. Geophys. Res.*, *92*(C7), 6787–6803, doi:10.1029/JC092iC07p06787.
- Tucker, W. B. III, and D. K. Perovich (1992), Stress measurements in drifting pack ice, *Cold Reg. Sci. Technol.*, *20*, 119–139, doi:10.1016/0165-232X(92)90012-J.
- Wang, Q., P. G. Myers, X. Hu, and A. B. Bush (2012), Flow constraints on pathways through the Canadian Arctic Archipelago, *Atmos. Ocean*, *50*(3), 373–385, doi:10.1080/07055900.2012.704348.
- Weeks, W. F., and A. J. Gow (1978), Preferred crystal orientations in the fast ice along the margins of the Arctic Ocean, *J. Geophys. Res.*, *83*(C10), 5105–5121, doi:10.1029/JC083iC10p05105.
- Weeks, W. F., and A. J. Gow (1980), Crystal alignments in the fast ice of Arctic Alaska, *J. Geophys. Res.*, *85*(C2), 1137–1146, doi:10.1029/JC085iC02p01137.
- Weiss, J., E. M. Schulson, and H. L. Stern (2007), Sea ice rheology from in-situ, satellite and laboratory observations: Fracture and friction, *Earth Planet. Sci. Lett.*, *255*, 1–8, doi:10.1016/j.epsl.2006.11.033.
- Wilchinsky, A. V., and D. L. Feltham (2006), Anisotropic model for granulated sea ice dynamics, *J. Mech. Phys. Solids*, *54*(6), 1147–1185, doi:10.1016/j.jmps.2005.12.006.
- Zhang, J., and W. D. Hibler III (1997), On an efficient numerical method for modeling sea ice dynamics, *J. Geophys. Res.*, *102*(C4), 8691–8702, doi:10.1029/96JC03744.